OPEN ACCESS

International
Journal
Of Modern Engineering Research (IJMER)

Investigation of Chirality Dependence of Carbon Nanotube-Based Ring Oscillator

Safura Sharifi[1], Yaser M. Banadaki[2]
[1]*College Of Science, Louisiana State University, Baton Rouge, LA 70803, U.S.A*
[2]*College Of Engineering, Southern University, Baton Rouge, LA 70813, U.S.A.*

ABSTRACT: *Carbon nanotube (CNT)-based integrated circuits including CNT field effect transistors (FET) and CNT interconnects are among promising emerging integrated circuits technology.In this paper, we have designed and simulated a single-walled CNT-based ring oscillator (RO) to investigate the chirality dependence of oscillation frequency using a numerical quantum-based model of CNT FET with 5 nm gate length and a compact diffusive model for CNT interconnects. Assuming contact resistance of 24KΩ, we have obtained oscillation frequency of 25 GHz, which reduces by ~%10 for every 1 nm increase in the diameter of zigzag CNT FET or 1µm increase in metallic CNT interconnects.*
Keywords:*carbon nanotube, ring oscillator, field effect transistors, interconnect.*

I. INTRODUCTION

The International Technology Roadmap for Semiconductors (ITRS)[1]has mentioned future technological challenges for scaling CMOS technology enforcing the semiconductor industry to explore the applications of novel materials and devices. The most promising alternatives for emerging integrated circuits have been categorized under carbon-based materials such as carbon nanotube (CNT) FET[2, 3] or graphene nanoribbon (GNR) FET[4, 5].A single-walled (SW) CNT is a rolled-up sheet of graphene discovered in 1991 by Iijima[6]. A SWCNT offers high mechanical strength, high carrier density, as well as high thermal and electrical conductivity. Since the discovery of carbon nanotubes researchers proposed various applications of this material ranging from device designing[7] to sensor applications [8, 9]. CNT FET has similar current-voltage characteristics as that of MOSFETs in silicon technology while the complementary design can be fabricated using identical transistors[7]. Carbon nanotubes can be either metallic or semiconducting depending on rolling direction. In an all-CNT circuit, the semiconducting and conducting CNTs are used for transistors and interconnects, respectively. The recent experimental reports [10, 11]reveal that the speed of CNT growth has the chirality dependence, such that they can be selectively grown with specific chirality. The selective and controllable fabrication of carbon nanotubes with specific chirality make all-CNT circuits promising design methodology, urging to be investigated in designing important integrated circuits[12, 13] such as the ring oscillator (RO), which is the purpose of this paper.

A ring oscillator is the ultimate test circuitry for new materials and a key building block in radio frequency, digital electronic and optical communication systems[14, 15]. Javey et al fabricated the first complementary SWCNT-based 3-stages RO with the CNT length and diameter of 3 µm and 2 nm obtaining the oscillation frequency of ~220 Hz[16]. IBM has announced the fabrication of high performance CNT-based 5-stages RO with the CNT length and diameter of 18 µm and 2nm, respectively, which results in oscillation frequency of 52 MHz[17]. A seven-stage CNT-based RO has also been proposed and simulated for the CNT FET with the gate length of 200 nm and the oscillation frequency of 3.75 MHz[7]. As Moore's law requires shrinking the channel length of transistors below 10 nm in next decade, it is important to predict and explore the characteristics of CNT-based integrated circuits with regard to physical parameters of CNT such as its chirality. At short-channel length, the simulation approach needs to consider the quantum confinement of the tube circumferential direction and quantum tunneling along the channel. The non-equilibrium Green's function (NEGF) formalism[18, 19] is a strength simulation method which fully treats the quantum phenomena, leading to a very accurate extraction of chirality dependence of few-nanometer CNT channels. For short-channel devices, the length of semiconducting CNT is usually less than its mean-free-path, which allows the assumption of ballistic carriers transport in CNT FETs. For interconnects in VLSI design, copper has much smaller mean-free path than a metallic CNT and suffers from electron surface scattering, grain-boundary scattering, electromigartion and void formation[20, 21]. Thus, both the metallic CNT interconnects and CNT FETs are promising for next-generation VLSI technology.

In this paper, we have investigated the chirality dependence of CNT-based ring oscillator using a numerical ballistic model for CNT FETs and a compact diffusive model for CNT interconnects. The paper is

organized as follows; in Section 2, the gate-all-around CNT FET structure has been modeled by solving the self-consistent problem between the Poisson and Schrödinger equations within the NEGF formalism. The current-voltage characteristics and corresponding voltage transfer characteristics of the CNT FET-based inverter have been obtained as a function of the chirality of few nanometer CNT channels. In section 3, the semi-classical model of CNT interconnect has been introduced for a metallic single-walled CNTs based on one-dimensional fluid model of electronic transport considering scattering mechanisms in long conducting CNT[21]. The metallic SWCNT interconnect is implemented by an equivalent transmission model consists of circuit elements distributed along its length including magnetic and kinetic inductance, quantum and electrostatic capacitances, and a non-linear resistance resulting from acoustic and optical phonon scatterings. Section 4 is devoted to the simulation of CNT-based RO circuits, where semiconducting and metallic CNTs have been used as transistors and interconnects between inverters, respectively. The obtained data from the device-level simulation of CNT FETs and the model of CNT interconnect have been introduced into SPICE circuit simulator. The multi-stage CNT-based RO has been simulated to explore the chirality dependence of the oscillation frequency as a fundamental physical parameter of CNT FETs and CNT interconnects in designing a CNT-based RO circuits.

II. DEVICE MODEL AND EQUATIONS

2.1 CNT FET Model

Fig. 1(a) shows a three-dimensional (3D) schematic view of the gate-all-around CNTFETs, where the semiconductor zigzag nanotube has been used in the channel with chirality n=3k+1 (k is positive integer)[12]. The source and drain regions are heavily doped and the metallic coaxial gate manipulates the carrier transport. The CNT FET was simulated by converging an iterative procedure, where the Poisson and Schrödinger equations are solved self-consistently[18, 19]. The transport problem in CNT channel can be accurately modeled using NEGF formalism, which can treat quantum-mechanical confinement, reflection, and tunneling[18]. The gate-all-around CNT transistor results in invariant potential and charge density around the nanotube. The electrostatic potential U_i along the CNT can be determined by 2D Poisson equation as follows:

$$\nabla^2 U_i(r,x) = -\frac{q}{\varepsilon}[p(x_i) - n(x_i) + N_D^+ - N_A^-] \qquad (1)$$

where N_D^+ and N_A^- are the doping profile of ionized donor and acceptor, respectively. $p(x_i)$ and $n(x_i)$ are hole and electron density distribution which are updated using the calculated NEGF formalism in iterative procedure. The retarded Green's function is given as follows:

$$G(E) = [(E + i\eta^+)I - H - \Sigma_S - \Sigma_D]^{-1} \qquad (2)$$

where E is the energy, η^+ is an infinitesimal positive value, I is the identity matrix and H is the Hamiltonian matrix for an isolated CNT channel. Σ_S and Σ_D are the self-energy matrices of the source and drain, which describe how the ballistic channel couples to the contacts. The mean-free-path of nanotube is around hundreds of nanometers at room temperature which allows near ballistic carriers transport. The carrier transport can be describe in mode space approach (using circumferential modes)[19]since the potential variation around coaxial-gated nanotube is small. The periodic boundary conditions $k_c C = 2\pi q$ mathematically allows to decouple the two dimensional nanotube lattice of a (n,0) zigzag nanotube into n-uncoupled one-dimensional mode space lattices as shown in Fig.1(b). In this equation, C is the circumference of the nanotube and q is the angular quantum number. This reduces the size of the Hamiltonian matrix and the corresponding computational cost. By constructing two different types of rings along the tube, the Hamiltonian matrix for the q^{th} subband can be calculated as follows:

$$H = \begin{bmatrix} U_1 & b_{2q} & & & \\ b_{2q} & U_2 & t & & 0 \\ & t & U_3 & b_{2q} & \\ & & \ddots & & \\ 0 & & t & U_{N-1} & b_{2q} \\ & & & b_{2q} & U_N \end{bmatrix}_{N\times N} \qquad (3)$$

where $b_{2q} = 2t\cos(\pi q/n)$ and t are coupling parameters between the nearest neighbor carbon rings, and N is the total number of carbon rings along CNT device. The diagonal elements Ui's are the electrostatic potential at the i^{th} carbon ring which obtained from Eq. (1). Corresponding to boundary conditions of the Schrödinger equation, the source self-energy matrix has only non-zero value in the (1, 1) element given as follows:

$$\Sigma_S(1,1) = \frac{(E-U_1)^2 + t^2 + b_{2q}^2 \pm \sqrt{[(E-U_1)^2 + t^2 + b_{2q}^2]^2 - 4(E-U_1)^2 t^2}}{2(E-U_1)} \qquad (4)$$

By replacing U_1 with U_N, the drain self-energy matrix with non-zero value in the (N, N) element can be calculated using an equation similar to Eq.(4). The level broadening of source and drain can be obtained using the self-energies of the corresponding contacts as follows:

$$\Gamma_{D(S)}(E) = i[\Sigma_{D(S)}(E) - \Sigma^{+}_{D(S)}(E)] \quad (5)$$

where $\Sigma^{+}_{D(S)}$ is the Hermitean conjugate of $\Sigma_{D(S)}$. The electron and hole correlation functions $G^{n(p)}(E)$ can be calculated as follows:

$$G^{n}(E) = G(E)\Sigma^{in}(E)G^{+}(E) \text{ and } G^{p}(E) = G(E)\Sigma^{out}(E)G^{+}(E) \quad (6)$$

where $\Sigma^{in}_{D(S)} = \Gamma_{D(S)} f_{D(S)}$ and $\Sigma^{out}_{D(S)} = \Gamma_{D(S)}(1 - f_{D(S)})$ are in(out) scattering functions for drain (source) contact couplings, respectively, which are the level broadening weighted by Fermi distribution function $f_{D(S)}$. The induced electron and hole distributions on carbon i^{th} ring can be calculated using the following equations:

$$n(x_i) = \frac{4}{\Delta x}\int_{E_m(j)}^{+\infty} \frac{G^{n}_{j,j}(E)}{2\pi} dE \text{ and } p(x_i) = \frac{4}{\Delta x}\int_{-\infty}^{E_m(j)} \frac{G^{p}_{j,j}(E)}{2\pi} dE \quad (7)$$

where E_m is the midgap energy and the factor of four is due to the two spin states and the twofold valley degeneracy. The calculated $p(x_i)$ and $n(x_i)$ have been applied to Poisson equation to calculate U_j^{new} and the corresponding Hamiltonian in the self-consistent iterative loop. Once the algorithm converges, the transmission coefficient T(E) and the corresponding current can be calculated as follows:

$$T(E) = \text{trace}(\Gamma_S(E)G(E)\Gamma_D G^{+}(E)) \quad (8)$$

$$I = \frac{4e}{h}\int_{-\infty}^{+\infty} T(E)[f(E - E_{FS}) - f(E - E_{FD})]\, dE \quad (9)$$

where h is the Plank constant, f is the Fermi-Dirac distribution and E_{FS} and E_{FD} are the Fermi energy levels in the source and drain regions. The details of the quantum transport calculation of CNT-based field effect transistor can be followed in[18, 19]. The drain-source currents of the proposed CNT FETs have been obtained using NEGF model for different chirality (n=3k+1) from 7 to 28. Figure 1(c) show the chirality dependence of drain current as a function of drain voltages. Increasing the chirality leads to the increase in drain-source current due to the contribution of more quantum channels.

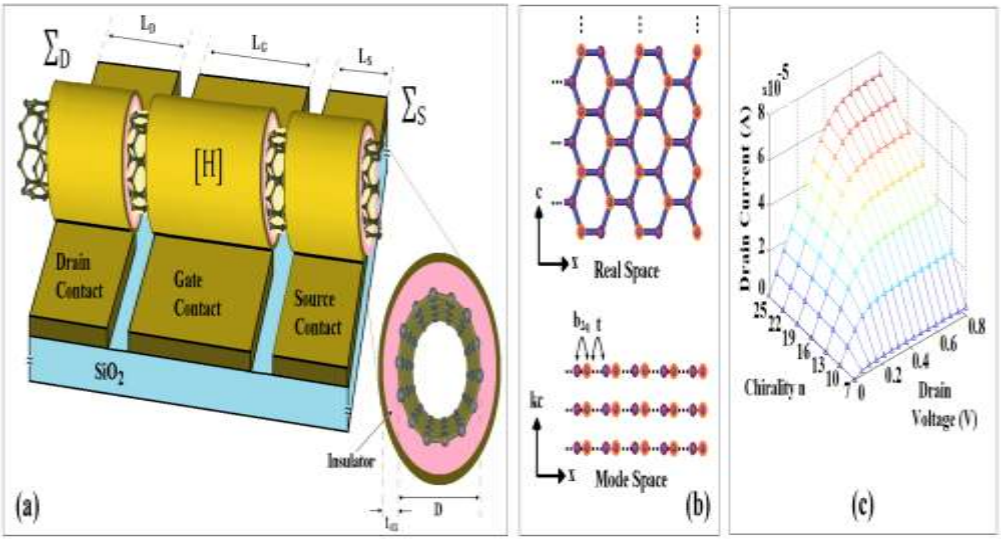

Fig.1. (a) 3-D schematic view of gate-all-around CNTFETs. L_D, L_G and L_S are the lengths of drain, gate and source where the spaces between the regions are due to visibility purpose and assumed zero in the simulations. t_{ox} and D are the insulator thickness and the diameter of semiconducting CNT corresponding to chirality n=3k+1 (k is positive integer), respectively. (b) Atomic configuration in real space and corresponding conceptual configuration in mode space approaches. The x arrows are the direction along the CNT FET device, c and kc are the circumferential directions in real space and reciprocal space, respectively. Coupling parameters between the nearest neighbor carbon rings in mode space are shown with t and b_{2q}, respectively.

2.2 CNT Interconnect Model

A metallic CNT has less problem with electromigartion and void formation and exhibits the high thermal and electrical conductivity as well as mechanical properties[20]. Electrons in copper interconnect not only have much less mean-free path than a CNT interconnect, but also suffer from electron surface scattering and grain-boundary scattering. This leads to the increase in the resistivity of a copper interconnects. The metallic CNT interconnects are promising alternative to current Cu interconnect in VLSI technology[1]. The equivalent circuit model of a metallic SWCNT isolated above a ground plane can be developed using one-dimensional fluid model [21]. This model consists of circuit elements distributed along its length as shown in Fig. 2(a). The inductance (L) consists of the series of magnetic inductance (L_M) and kinetic inductance (L_K). The magnitude of magnetic inductance is logarithmically sensitive to the ratio of distance between nanotube and the ground (t_{ins}) as well asthe nanotube diameter (D_{in}) as follows:

$$L_M = \frac{\mu}{2\pi}\ln\left(\frac{t_{ins}}{D_{in}}\right) \quad (10)$$

The kinetic inductance is dominant inductance with several orders of magnitudes and thus plays a vital role in high frequency applications. This is in contrary to macroscopic long thin wires with relatively larger magnetic inductance. The kinetic inductance is as follows:

$$L_k \approx \frac{\pi\hbar}{e^2 v_F} \quad (11)$$

where$\hbar$ is reduced Plank constant. The capacitance also consists of quantum capacitance of the nanotube and electrostatic capacitance between a wire and a ground plane. The quantum capacitance is due to the Pauli's exclusion principle in quantum electron gas of a metallic SWCNT interconnect as follows:

$$C_Q \approx \frac{e^2}{\pi\hbar v_F} \approx 100\ \text{aF}/\mu\text{m} \quad (12)$$

Similar to the magnetic inductance, the electrostatic capacitance depends on the insulator thickness and nanotube diameter while its contribution to equivalent capacitance is important and given as follows:

$$C_E \approx \frac{2\pi\varepsilon}{\ln\left(\frac{t_{in}}{D_{in}}\right)} \quad (13)$$

The increase of equivalent capacitance as a function of chirality is shown in Fig 2(b). The resistance in the equivalent transmission model has the voltage (V) and diameter (D_{in}) dependence, which can be determined by the effective mean free path of electron in a metallic SWCNT interconnect (λ_{eff}) considering acoustic and optical phonon scattering mechanisms. The spontaneous scattering lengths for emitting an optical phonon (λ_{op}) and acoustic phonon (λ_{ac}) have diameter dependence, which can be estimated as follows[3]:

$$\lambda_{op} = 56.4\ D_{in} \quad (14)$$

$$\lambda_{ac} = \frac{400.46\times10^3 D_{in}}{T} \quad (15)$$

In order to calculate the effective mean free path, three scattering lengths needs to be calculated for optical phonon scattering, which are optical phonon absorption ($\lambda_{op,abs}$), optical phonon emission for the absorbed energy ($\lambda^{abs}_{op,ems}$), and optical phonon emission for the electric field across the SWCNT length ($\lambda^{field}_{op,ems}$) as follows[8]:

$$\lambda_{op,abs} = \lambda_{op}\frac{N_{op}(300)+1}{N_{op}(T)} \quad (16)$$

$$\lambda^{abs}_{op,ems} = \lambda_{op,abs} + \frac{N_{op}(300)+1}{N_{op}(T)+1}\lambda_{op} \quad (17)$$

$$\lambda^{field}_{op,ems} = \frac{\hbar\omega_{op} - K_B T}{q\frac{V}{L_{in}}} + \frac{N_{op}(300)+1}{N_{op}(T)+1}\lambda_{op} \quad (18)$$

where$N_{op} = 1/\left[1+\exp(\hbar\omega_{op}/K_B T)\right]$ is the optical phonon occupation in Bose-Einstein statistics, K_B is the Boltzman constant, $\hbar\omega_{op}$ is optical phonon energy and L_{in} is the CNT interconnect length. Finally, the effective mean free path and the corresponding resistance can be calculated by Matthiessen's rule as follows:

$$\frac{1}{\lambda_{eff}} = \frac{1}{\lambda_{ac}} + \frac{1}{\lambda^{abs}_{op,ems}} + \frac{1}{\lambda^{field}_{op,ems}} + \frac{1}{\lambda_{op,abs}} \quad (19)$$

$$R(V, D_{in}) = \frac{R_0}{4}\frac{L_{in}}{\lambda_{eff}} \quad (20)$$

where $R_0 \approx \pi\hbar/2e^2 \approx 12.9\ k\Omega$ is quantum resistance. Figure 2(c) shows the voltage and diameter (interconnect chirality) dependence of the resistance in the equivalent transmission model for a CNT interconnect with the length of$L_{in} = 1\ \mu m$. The calculated resistance of a SWCNT interconnect is highly sensitive to the value of voltage across the tube, in which the dependence increases by decreasing chirality. The increase in chiral value leads to the increase in the number of energy bands in energy-wavevector diagram, enhancing the current capability of the metallic CNT. By increasing chiral value, the equivalent capacitance increases while the resistance decreases depending on voltage across the tube, resulting in a RC delay.

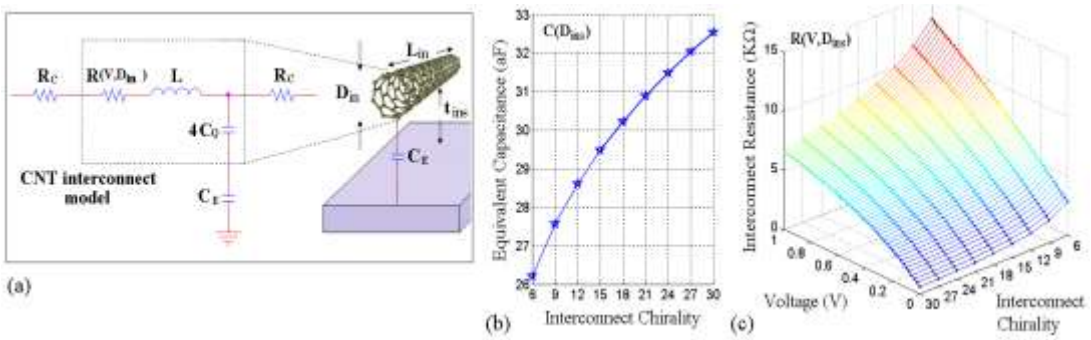

Fig.2.(a) Transmission line model of a SWCNT interconnect. The inductance (L) consists of the series of magnetic (L_M) and kinetic (L_K) inductances. C_E andC_Q are the electrostatic and quantum capacitance. $R_c$is the contact resistance, which is assumed equal to zero in Figs. 5, 6(a), and 6(b) while its dominant effect is investigated in Fig. 6(c). $R(V, D_{in})$ is the resistance of CNT interconnect which depends on voltage across the interconnect and CNT diameter, (b) Equivalent capacitance of a CNT interconnect with the length of $L_{in} = 1\ \mu m$ as a function of chirality (n,n) and (c) Resistivity of a CNT interconnect with the length of $L_{in} = 1\ \mu m$ as a function of voltages and its chirality (n,n).

III. ALL-CNT RING OSCILLATOR

By intersecting the current-voltage characteristics of n- and p-type CNT FETs obtained from numerical simulations, the voltage transfer characteristic (VTC) of complementary CNT FET-based inverter can be obtained as a function of chirality as shown in Fig. 3(b). The VTC curves of low-chirality CNT FETs have sharp transition from ON-state to OFF-state while the non-linearity in VTC curves decreases by increasing chirality of CNT FETs. The current of CNT FET-based inverter as a function of input voltage has been shown in Fig. 3(b). Increasing the chirality from 7 to 28 leads to four orders of magnitude increase in the maximum current of inverter from $\sim 5.7 \times 10^{-9} A$to $\sim 4.2 \times 10^{-5} A$.

In a ring oscillator, the input of each inverter is the output of the previous inverter, closing the ring by returning the output of the last inverter to the first stage. The cascade combination of inverters results in sequentially change of logic state and the corresponding oscillation depending on propagation delay (t_p) in voltage switching between successive inverter stages. Fig. 4(a) shows the schematic of the multi-stage RO, where semiconducting and metallic CNTs have been used as transistors and interconnects between inverters, respectively. The developed analytical or numerical model of a nanometer device and interconnect can be incorporated in SPICE using Verilog-AMS[22] or SPICE elements[23]. We have incorporated the device-level data of CNT FET-based VTC curve and the non-linear resistance of CNT interconnects using SPICE elements named GTABLE and ETABLE [23]as shown in Fig. 4(b).

Figure 5(a) shows the output waveforms and its Fourier transform of 3-stages CNT-based RO for CNTFET (7, 0) and CNT interconnect (27, 27). The circuit has a large signal oscillation at about 220 GHz and the odd components are dominant in the frequency spectrum of the signal. The frequency of a RO is given by $f = 1/(2t_pN)$, where N is the number of stages.The proposed RO has three stages (N=3), which results in an average propagation delay of 0.75 pico-second for each stage.The small propagation delay of an inverter stageis due to the assumption of perfect electrode contacts ($R_c = 0$), short channel length of CNT FET ($L_G = 5\ nm$)[16]. The oscillation frequency decreases by increasing CNT FET chirality as shown in Fig 5(b). The oscillation frequency of 3-stage RO has been obtained ~250 GHz, which reduces to ~215 GHz for changing CNT chirality from n=7 to 28. The CNT diameter can be related to its chirality by $d = \sqrt{3}a_{cc}n/\pi$, where $a_{cc} = 0.142\ nm$ is inter-atomic distance between two nearest-neighbor carbon atoms. Thus, the oscillation

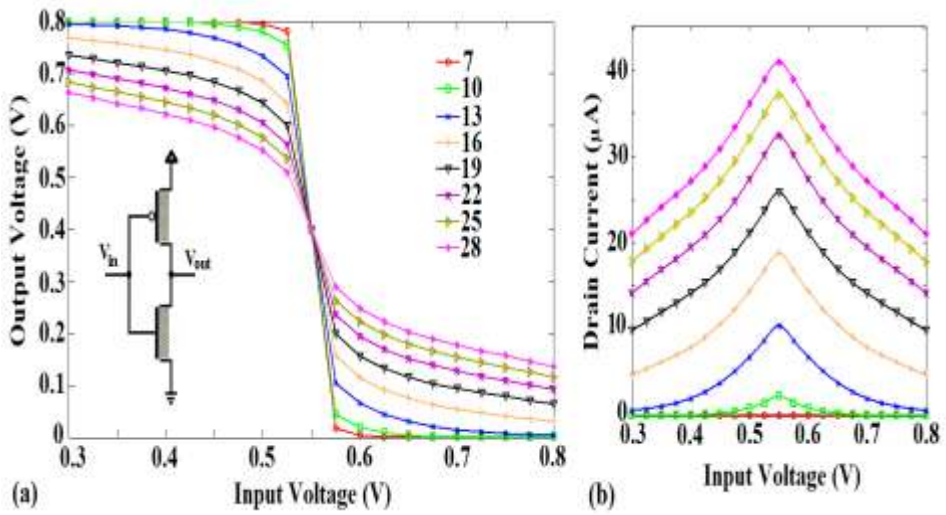

Fig.3. (a) Voltage transfer characteristic of CNTFET-based inverter using NEGF model for different chirality (n,0), (b) Current of CNTFET-based inverter as a function of input voltage for different chirality (n,0). Note: The device geometries and parameters of the CNT FETs are kept as mentioned in Fig. 2.

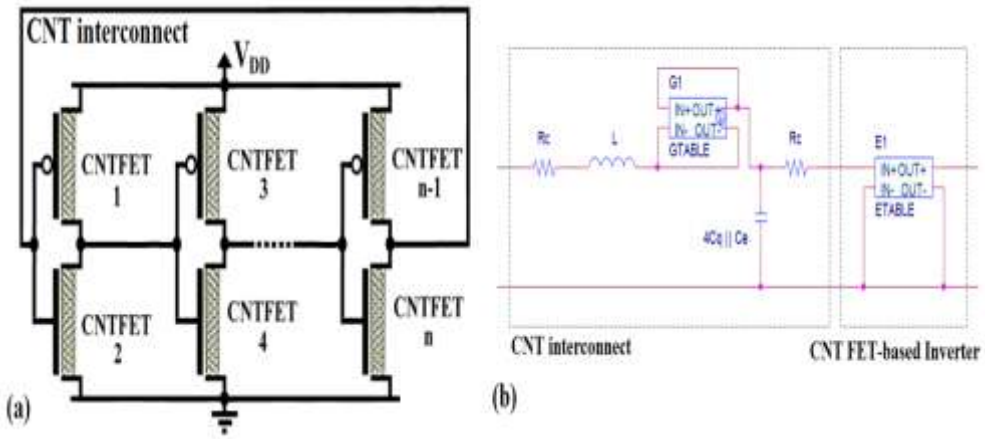

Fig.4. (a) Circuit schematic of multi-stage CNT-based ring oscillator and (b) SPICE schematic of CNT interconnect and CNT FET-based inverter showing the correct connection of GTABLE and ETABLE elements.

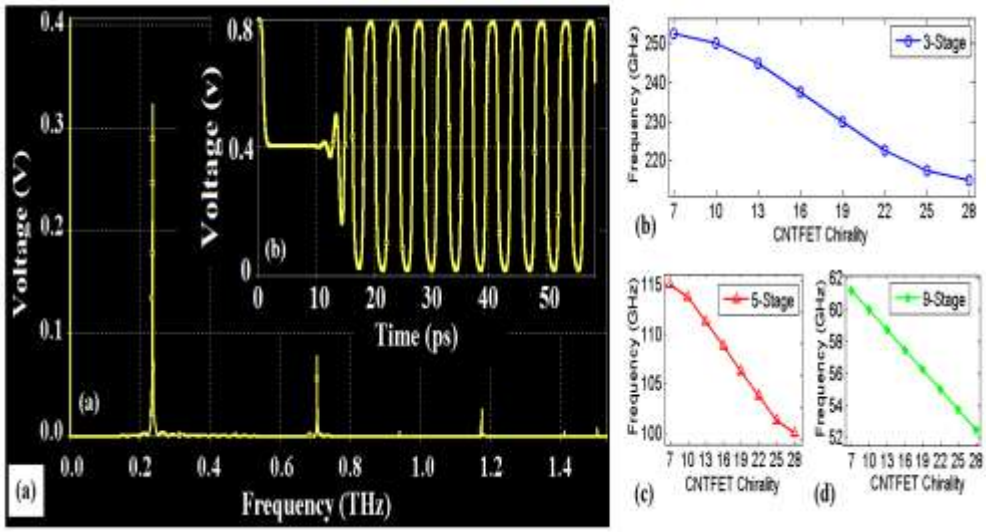

Fig.5.(a) Output waveforms and its Fourier transform of 3-stage CNT-based RO for CNTFET (7,0) and CNT interconnect (27,27). The oscillation frequency of CNT-based RO as a function of chirality for ring

oscillators with (b) three, (c) five and (d) nine stages.Note: The simulation parameters are$L_D = L_G = L_S$ =5nm, $t_{ox} = 2nm$, $L_{in} = 100$ nm, and$\varepsilon_{ox} = 16$. (For graph in part (a), all the parameters are same except $\varepsilon_{ox} = 4$).

Frequency is reduced by % 8.5 per 1 nm increase in diameter of zigzag CNT. The oscillation frequency is determined by the propagation time delay of CNT-based inverter stages and by the number of stages used in thering. The latter creates the multi-phase outputs as each stage provides a phase shift of π/m, where m is number of stages. Figure 5(b) and 5(c) show the frequency of CNT-based RO as a function of chirality for ring oscillators with m = 5 and m = 9, respectively. For all three types of ring oscillators, the oscillation frequency is decreased by increasing the CNT chirality. However, the trends are different as the change of frequency by chirality becomes more linear for ring oscillator with higher number of stages.

Figure 6(a) shows the oscillation frequency of 3-stage CNT-based ring oscillator as a function of CNT FET chirality for different dielectric thicknesses (t_{ox}). The other circuit parameters as well as the chirality of CNT interconnect have been kept constant in the simulation. For $t_{ox} = 1$ nm, the oscillation frequency decreases from 245 GHz to 217 GHz by increasing CNT FET chirality form n = 7 to 22 (blue curve). For CNT FET chirality more than n = 25, CNT-based RO stop oscillating because of reducing the non-linearity of VTC curves of CNT-based inverters. By increasing the dielectric thickness, the non-oscillation chirality have been shiftedto lower values as n =19, 16, and 13 corresponding to the dielectric thickness of $t_{ox} = 1.5$nm, 2nm and2.5 nm, respectively.The oscillation frequency is more sensitive to CNT FET chirality for higher dielectric thickness resulting in higher reduction of frequency from n = 7 to n = 10 at $t_{ox} = 2.5$nm (black curve). Also, at the same chirality of n = 7, the oscillation frequency of 245 GHz at $t_{ox} = 1$ nm decreases to ~232 GHz at $t_{ox} = 2.5$ nm due to the reduction of gate controllability on the modulation of CNT FET channel. Figure 6(b) shows the frequency of 3-stage CNT-based RO as a function of CNT FET chirality for the dielectric constants of $\varepsilon_{ox} = 10, 16$ and 25[24]. For $\varepsilon_{ox} = 10$, the oscillation frequency decreases from 250 GHz to 215 GHz by increasing CNT FET chirality form n = 7 to 28 (blue curve). Increasing the dielectric constant shifts the curve to higher oscillation frequencies.

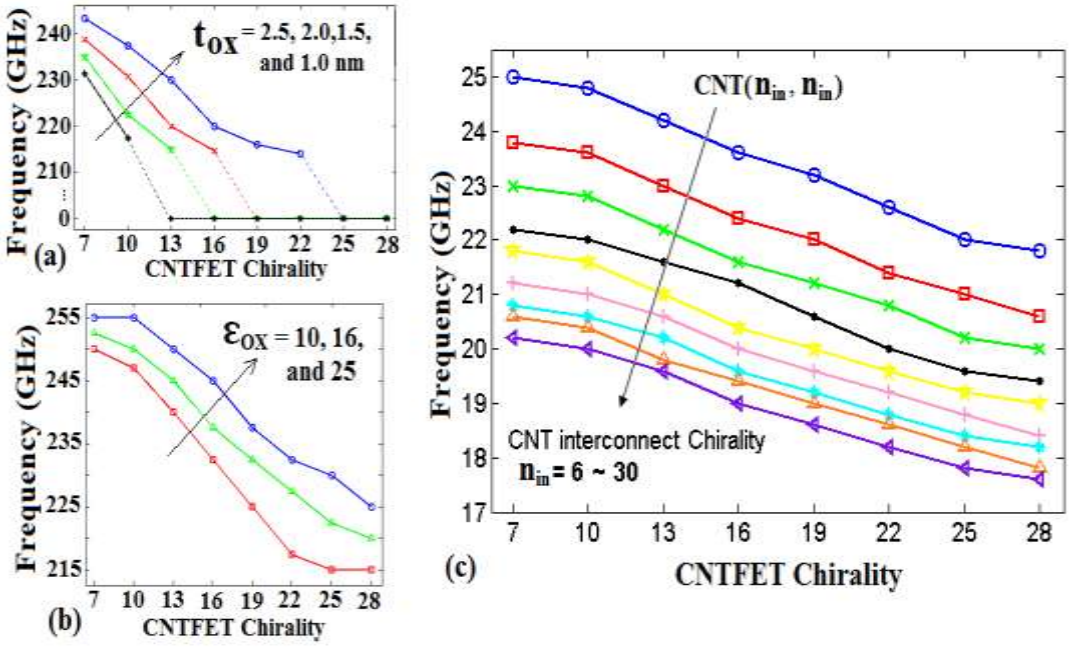

Fig.6. Oscillation frequency of 3-stage CNT-based ring oscillator as a function of chirality for (a)different dielectric thicknesses when the dielectric constant of CNTFETs are set$\varepsilon_{ox} = 4$, and (b) different dielectric constants when the dielectric thickness of CNTFETs are $t_{ox} = 2nm$. (c) Oscillation frequency of 3-stage CNT-based RO as a function of chirality for ring oscillators for a conducting CNT interconnect with different chiralities when the contact resistance is set equal to$R_c = 24$KΩ.The simulation parametersin (c) are$L_D = L_G = L_S$ =5nm,$t_{ox} = 2$ nm, $\varepsilon_{ox} = 16$, $L_{in} = 1$μmand $n_{in} = 27$.

Until now, we have assumed a perfect electrode contacts ($R_c = 0$) in the model shown in Fig. 2(a) to provide a proof-of-concept for the chirality dependence of oscillation frequency regardless of total contact resistance ($2R_c$) of a single-walled CNT which has been reported different values between 10 kΩ to 100 kΩ for Pt electrodes[25]. Figure 9 shows the frequency of 3-stage CNT-based RO as a function of CNT FET chirality

for different chirality indices of CNT interconnects, in which the contact resistance is assumed $R_c = 24K\Omega$. Taking into account contact resistances, there is an order of magnitude reduction in the oscillation frequency. However, the trend of frequency reduction as a result of increasing the CNT FET chirality remains the same as in the case of perfect electrode contacts in the previous simulations. Increasing the chirality of SWCNT interconnect also reduces the oscillation frequency same as the effects of increasing the CNT FET chirality. The oscillation frequency reduces from 25 GHz to 22 GHz for increasing the CNT FET chirality from n = 7 to 28 with the constant chirality of CNT interconnect $n_{in} = 27$ and with the length of $L_{in} = 1\mu m$ between inverter stages. Similarly, the oscillation frequency reduces from 25 GHz to 20.3 GHz for increasing the chirality of SWCNT interconnects from $n_{in} = 6$ to 30 with the constant CNT FET chirality of n = 7. The reduction of oscillation frequency has been estimated by ~10% per 1 nm increase in diameter of $1\mu m$ metallic CNT interconnects.

IV. CONCLUSION

We have designed and simulated a carbon nanotube-based ring oscillator, where semiconducting and metallic CNTs have been used as transistors and interconnects between inverters, respectively. We have investigated the chirality dependence of the proposed ring oscillator using a numerical ballistic model based on NEGF formalism for CNT FETs with the gate length of 5 nm and a compact diffusive model for CNT interconnects. We have found that the oscillation frequency of all 3-, 5-, and 7-stages CNT-based ring oscillator decreases by increasing the chirality of both (n, 0) CNT FETs and (n, n) CNT interconnects while the trends becomes more linear by increasing the number of stages. The frequency reduction has been estimated by ~10% per 1 nm increase in diameter of 1μm metallic CNT interconnects. We have found that the oscillation frequency is reduced by increasing dielectric thickness and decreasing dielectric constant leading to the lack of oscillation for high-chirality CNTFETs. Assuming the contact resistance of $R_c = 24K\Omega$, the oscillation frequency of ~25 GHz has been obtained for 5 nm (7, 0) zigzag CNT FETs and 1μm (6, 6) metallic CNT interconnects. This indicates the importance of contact resistance in the performance of CNT-based circuits. As the fabrication technology of short channel CNTFETs and CNT interconnect is still in an early stage, this work provide designer with a performance evaluation of an CNT-based circuits with regard to CNT chirality and contact resistance in fabrication process.

REFERENCES

[1]. I. Committee, International technology roadmap for semiconductors, edition 2013.

[2]. A. Graham, G. Duesberg, W. Hoenlein, F. Kreupl, M. Liebau, R. Martin, et al., How do carbon nanotubes fit into the semiconductor roadmap?, Applied Physics A 80(6), 2005, 1141-1151.

[3]. A. D. Franklin and Z. Chen, Length scaling of carbon nanotube transistors, Nature nanotechnology, 5(12), 2010, 858-862.

[4]. Y. M. Banadaki and A. Srivastava, Scaling Effects on Static Metrics and Switching Attributes of Graphene Nanoribbon FET for Emerging Technology, IEEE Transactions on Emerging Topics in Computing, 3(4) , 2015, 458-469.

[5]. Y. M. Banadaki, Physical Modeling of Graphene Nanoribbon Field Effect Transistor Using Non-Equilibrium Green Function Approach for Integrated Circuit Design, doctoral diss., Louisiana State University, Baton Rouge, 2016.

[6]. S. Iijima, Helical microtubules of graphitic carbon, nature,354(6348), 1991, 56-58.

[7]. S. Fregonese, C. Maneux, and T. Zimmer, A compact model for dual-gate one-dimensional FET: application to carbon-nanotube FETs, IEEE Transactions on Electron Devices, 58(1), 2011, 206-215.

[8]. K. Mohsin, Y. Banadaki, and A. Srivastava, Metallic single-walled, carbon nanotube temperature sensor with self heating, Proc. SPIE 9060, Nanosensors, Biosensors, and Info-Tech Sensors and Systems, San Diego, CA, 2014, 906003-7.

[9]. Y. M. Banadaki, A. Srivastava, and S. Sharifi, Metallic single-walled carbon nanotube for ionized radiation detection, Proc. SPIE 9802, Nanosensors, Biosensors, and Info-Tech Sensors and Systems, 2016, 98020A-9.

[10]. R. Rao, D. Liptak, T. Cherukuri, B. I. Yakobson, and B. Maruyama, In situ evidence for chirality-dependent growth rates of individual carbon nanotubes, Nature materials,11(3), 2012, 213-216.

[11]. K. K. Koziol, C. Ducati, and A. H. Windle, Carbon nanotubes with catalyst controlled chiral angle, Chemistry of Materials,22(17), 2010, 4904-4911.

[12]. A. D. Franklin, S. O. Koswatta, D. B. Farmer, J. T. Smith, L. Gignac, C. M. Breslin, S.-J. Han, G. S. Tulevski, H. Miyazoe, and W. Haensch, Carbon nanotube complementary wrap-gate transistors, Nano letters,13(6), 2013, 2490-2495.

[13]. D. Dass, R. Prasher, and R. Vaid, Single Walled CNT Chirality Dependence for Electrical Device Applications, The African Review of Physics,8, 2013.

[14]. M. Mandal, and B. Sarkar, Ring oscillators: Characteristics and applications, Indian journal of pure & applied physics,48, 2010, 136-145.

[15]. S. Docking, and M. Sachdev, An analytical equation for the oscillation frequency of high-frequency ring oscillators, IEEE Journal of Solid-State Circuits, 39(3), 2004, 533-537.

[16]. A. Javey, Q. Wang, A. Ural, Y. Li, and H. Dai, Carbon nanotube transistor arrays for multistage complementary logic and ring oscillators, Nano Letters,2(9), 2002, 929-932.
[17]. Z. Chen, J. Appenzeller, P. M. Solomon, Y.-M. Lin, and P. Avouris, High performance carbon nanotube ring oscillator, Proc. of IEEE 64th Device Research Conference, 2006, 171-172.
[18]. Z. Arefinia, and A. A. Orouji, Quantum simulation study of a new carbon nanotube field-effect transistor with electrically induced source/drain extension, IEEE Transactions on Device and Materials Reliability,9(2), 2009, 237-243.
[19]. J. Guo, S. Datta, M. Lundstrom, and M. Anantam, Toward multiscale modeling of carbon nanotube transistors, International Journal for Multiscale Computational Engineering,2(2), 2004, 1-21.
[20]. F. Chen, A. Joshi, V. Stojanović, and A. Chandrakasan, Scaling and evaluation of carbon nanotube interconnects for VLSI applications, Proc. of the 2nd international conference on Nano-Networks, Brussels, Belgium, 2007, 1-24.
[21]. A. Srivastava, Y. Xu, and A. K. Sharma, Carbon nanotubes for next generation very large scale integration interconnects, Journal of Nanophotonics,4(1), 2010, 041690-26.
[22]. S. Das, S. Bhattacharya, and D. Das, Modeling of carbon nanotube based device and interconnect using VERILOG-AMS, 3rd International Conference onAdvances in Recent Technologies in Communicationand Computing, Bangalore, india, 2011, 51-55.
[23]. M. J. Sharifi, and Y. M. Banadaki, A SPICE large signal model for resonant tunneling diode and its applications, AIP Conf. Proc. 1148, Hersonissos, Greece, 2009, 890-893.
[24]. A. Srivastava, Y. M. Banadaki, and M. S. Fahad, "(Invited) Dielectrics for Graphene Transistors for Emerging Integrated Circuits," ECS Transactions, 61(2), 2014, 351-361.
[25]. E. Pop, D. A. Mann, K. E. Goodson, and H. Dai, Electrical and thermal transport in metallic single-wall carbon nanotubes on insulating substrates, Journal of Applied Physics, 101(9), 2007, 093710.